Energy Reports 7 (2021) 1460–1472

Contents lists available at ScienceDirect

Energy Reports

journal homepage: www.elsevier.com/locate/egyr

Machine and deep learning for estimating the permeability of complex carbonate rock from X-ray micro-computed tomography

Moussa Tembely *, Ali M. AlSumaiti, Waleed S. Alameri

Khalifa University of Science and Technology, Abu Dhabi, United Arab Emirates

ARTICLE INFO

Article history:
Received 24 November 2020
Received in revised form 15 February 2021
Accepted 22 February 2021
Available online 10 March 2021

Keywords:
Flow in porous media
Digital rock physics
Carbonate rock
Machine learning
Deep learning

ABSTRACT

Accurate estimation of permeability is critical for oil and gas reservoir development and management, as it controls production rate. After assessing numerical techniques ranging from pore network modeling (PNM) to the lattice Boltzmann method (LBM), an AI-based workflow is developed for a quick and accurate estimation of the permeability of a complex carbonate rock from its X-ray micro-computed tomography (micro-CT) image. Following features engineering using both image processing and PNM, we trained and tested the workflow on thousands of segmented 3D micro-CT images using both shallow and deep learning algorithms to assess the permeability. A broad variety of supervised learning algorithms are implemented and tested, including linear regression, support vector regression, improved gradient boosting, and convolutional neural networks. Additionally, we explored a hybrid physics-driven neural network that takes into account both the X-ray micro-CT images and petrophysical properties. Finally, we found that the predicted permeability of a complex carbonate by machine learning (ML) agrees very well with that of a more computationally-intensive voxel-based direct simulation. In addition, the ML model developed here provides a substantial reduction in computation time by roughly three orders of magnitude compared to that of the LBM. This paper highlights the crucial role played by features engineering in predicting petrophysical properties by machine and deep learning. The proposed framework, integrating diverse learning algorithms, rock imaging, and modeling, has the potential to quickly and accurately estimate petrophysical properties to aid in reservoir simulation and characterization.

1. Introduction

Predicting the properties of routine core and special core analysis is essential to make accurate reservoir descriptions, with direct impacts on enhanced oil recovery (EOR) strategy, completion designs, and reservoir management. Oil & gas industry is fast-paced and has vast amounts of data, making it a prime candidate for a data-driven approach. Efficient estimation of petrophysical properties is critical in reservoir characterization and production (Davarpanah et al., 2018; Hu et al., 2020). Owing to inherent heterogeneities existing at both observational and measurement scales, characterization of carbonate reservoirs is still very difficult (Andrä et al., 2013). The permeability, which represents a feature of pore space microstructure and the capacity of a rock to transmit fluid, is one of the most essential properties for porous media characterization. In oil & gas industry, knowledge of the permeability is essential in targeting a desired commercial oil and gas production rate (Davarpanah et al., 2018; Ling, 2012). Since there is no universal relationship for permeability, efficient tools to estimate it are desirable and are the subject of ongoing research (Ling, 2012; Chung et al., 2019; Dehghan Khalili et al., 2013; Tembely et al., 2020; Davarpanah et al., 2020).

Darcy-scale reservoir petrophysical properties are controlled by the pore-scale flow properties, and numerical simulation is the only practical methodology for upscaling from pore to Darcy scale. However, one of the shortcomings of pore-scale imaging and modeling is the computational power required to carry out accurate simulations. Numerical computation of petrophysical properties at pore scale, such as flow and elastic properties, can be broken down into two families: (i) pore-network modeling (Dong and Blunt, 2009) and (ii) direct modeling, which encompasses the finite difference method (Mostaghimi et al., 2013; Blunt et al., 2013), the finite element method (Andrä et al., 2013; Sun et al., 2020), the finite volume method (Guibert et al., 2015; Tembely et al., 2017), the smoothed-particle hydrodynamics method (Pereira et al., 2011), and the lattice Boltzmann method (LBM) (Blunt et al., 2013). Due to its simplicity, pore network modeling (PNM) is preferred instead of more intensive direct simulation to predict petrophysical properties. However, the PNM approach, which is based on simplifying the geometry

* Corresponding author.
E-mail addresses: moussa.tembely@concordia.ca, moussa.tembely@ku.ac.ae (M. Tembely).

https://doi.org/10.1016/j.egyr.2021.02.065

of the pore space, does not provide reliable estimations. To overcome the limitations inherent to PNM, machine and deep learning algorithms were developed to achieve fast and efficient computation of the permeability. The proposed workflow could be expanded to computation of other petrophysical properties based on 3D images, such as the estimation of elastic and multiphase flow properties.

Machine learning (ML), with its potential to regularize, generalize, and analyze complex interactions, has gained renewed interest within the artificial intelligence (AI) field in recent years (Serre, 2019). It has been applied to tackle many academic research and industrial challenges including fluid dynamics (Brunton et al., 2020), petroleum engineering (Kohli and Arora, 2014; Alkinani et al., 2019), and medical diagnostics (Yala et al., 2019; Chilamkurthy et al., 2018). However, the majority of AI applications in the oil & gas industry are focused on rock typing and classification (Mandal and Rezaee, 2019), estimation of well-log properties, and, very recently, optimization of well placement and drilling (Pollock et al., 2018; Nwachukwu et al., 2018). There have been very few studies dedicated to estimating petrophysical properties based on 3D micro-CT scans. Although deep neural networks provide vastly improved predictive capabilities in complex problems, little effort has been devoted to applying them to digital rock physics (DRP) in order to estimate and potentially speed up the computation of petrophysical properties. Recently, Sudakov et al. (2019) attempted to estimate permeability using machine learning (ML); however, the model depends on the less reliable and generally inaccurate PNM simulations as the output (or target) of the ML model. In addition, the analysis and incorporation of petrophysical features engineering were not considered. Finally, in Wu et al. (2018), ML is used to predict the permeability based on simple 2D synthetic images, which do not correspond to actual reservoir rock. Similarly, in Araya-Polo et al. (2020) 2D thin sections images from 11 clastic reservoirs are used to estimate permeability using convolutional neural network (CNN). In the same line, it is worth mentioning the recent work by Wang et al. (2020) using CNN to estimate the diffusivity based on porous media reproduced via a stochastic reconstruction method. An interesting approach using ML is developed in Miao et al. (2017) to accurately estimate hydraulic conductances based on a number of pore shape or geometric parameters. Their ML model is trained and tested on 2D carbonate and sandstone images. The estimated hydraulic conductances are found to be around 90% within 20% error bounds. Nonetheless, the assessment of the permeability for 3D geometry still remains to be addressed. However, compared to the current approach focused on simplifying pore space, a workflow relying on actual rock pore space is expected to improve permeability predictions. In Rabbani and Babaei (2019) a pore network geometry in combination with the LBM is investigated. Because of its precision, the LBM is employed to compute the permeability from the pore-throat network, which is more accurate than the classical Hagen–Poiseuille equation adopted by PNM. The overall computational cost is minimized by employing image-based features to assess LBM throat permeabilities in conjunction with ML. In order to reduce LBM computational cost, a graphics processing unit-accelerated LBM based on phase-field formalism is developed in Alpak et al. (2019) to simulate two-phase flow from X-ray microtomography images. The model was able to capture phenomena including snap-off, Haines jumps, and capillary desaturation.

Despite the extensive use of PNM in pore-scale modeling, the method exhibits certain inherent limitations in predicting petrophysical properties from 3D micro-CT images. One of the drawbacks of PNM is that the model relies on a simplified pore-space to describe fluid flow through (more or less complex) porous media. In order to remediate these shortcomings, it is essential to directly solve the flow governing equations in a pore geometry without any simplification. However, due to the high computational cost of the LBM (Alpak et al., 2019; Rabbani and Babaei, 2019), it is challenging to account for all the relevant physical processes and the microstructure of the pore space (Xie et al., 2016). It should be noted that the current techniques to estimate the permeability at pore-scale can be classified into direct and indirect methods. LBM is considered as a direct method where simulations are performed directly on segmented images, corresponding to the pore space without uncertainties related to meshing, whereas PNM uses a simplified geometry limiting its predictive capability and accuracy.

Due to the high computational cost of direct simulations, in most pore-scale modeling, the permeability is computed using PNM and considered to be the actual permeability of the sample or micro-CT image. However, as we demonstrate in the present paper, there is a substantial difference between the permeability derived from the more accurate voxel-based LBM approach and PNM. This discrepancy is more pronounced in the present case for complex carbonate rock unlike in our previous work dedicated to simple sandstone rock (Tembely et al., 2020). In that context, machine and deep learning could be an attractive alternative for efficiently estimating permeability from images.

In this paper, we employ X-ray micro-CT images of complex carbonate rock from the Middle East to assess a comparative analysis of three numerical techniques used to compute permeability in the context of pore-scale modeling. By using the maximal ball algorithm, a pore network is first created from the binary 3D image and the simplified pore space is then used as an input to the PNM simulation to calculate the formation resistivity factor and permeability of sample. Additionally, considering the same segmented (or binary) images, more complex pore geometry is generated and meshed in order to perform the finite volume method (FVM) computation of the permeability. Last, a voxel-based approach based on LBM is used to compute the permeability directly from the segmented 3D images. Overall, the high computational cost of the simulation is closely linked to the complexity of the pore-space microstructure, while its accuracy is dictated by the degree of simplification of the pore space, which is the case for PNM. Finally, a machine and deep learning workflow utilizing thousands of X-ray micro-CT images is developed for efficient computation of the permeability. The ultimate objective is to provide an effective data-driven (machine and deep learning) and physics-based (FVM, PNM, LBM) models capable of estimating fast and accurately the permeability for complex carbonate rock.

The paper is organized by starting with the features engineering through simulation in Section 2, and continuing to the application of machine learning to the generated features for prediction in Section 3. Finally, conclusions are drawn in Section 4

2. Computation of fluid flow properties

In order to estimate flow properties, we have combined ML and numerical simulations to model fluid flow behavior within a 3D digital porous rock, obtained from X-ray microtomography (Fig. 1). However, to avoid bias related to the segmentation techniques, segmented images are used as inputs for the permeability estimation for both the LBM and machine learning approaches. An automated segmentation technique based on Otsu's method was used to segment the grayscale micro-CT image for convenience. In this paper, we mainly focused on the estimation of the permeability, which could be regarded as a complex function of many variables, such as the porosity, the rock type, and the geometry of the pore space, in addition to the connection and distribution of the different pores. The framework developed here can aid in

Fig. 1. Segmented 3D micro-CT image, with size of 500 × 500 × 920 voxels at 0.48 μm resolution, of a complex carbonate sample used for applying the machine and deep learning workflow.

establishing cost-effective and efficient modeling for estimation of permeability in rocks.

Supervised linear regression, tree-based, and deep learning algorithms are trained, tested, and validated on a dataset generated using two widely-employed numerical approaches, namely network modeling and voxel-based direct simulation. Three numerical methods are used to achieve this: PNM, FVM, and LBM. These techniques are detailed below.

2.1. Permeability computed by PNM

Taking as input a 3D segmented micro-CT image, PNM can be used to estimate the permeability from images. The PNM model simulates a pore space consisting of a pore and throat network that topologically corresponds to the pore geometry of the core plug scanned at high resolution. Using the Hagen–Poiseuille relation, the flow rates (Q_{ij}) within the throats between pores are given by:

$$Q_{ij} = -\frac{{r_{ij}}^2}{8\mu l_{ij}}(p_j - p_i) \tag{1}$$

where p_i and p_j are the pressures at nodes i and j, l_{ij} is the pore throat length, r_{ij} is the pore-throat radius, and μ is the viscosity. The PNM simulations are performed on pore networks generated by the maximal ball algorithm based on X-ray micro-CT of the rock sample. Following the resolution of the continuity equation and using Darcy's law, the permeability can be expressed as follows:

$$K = \frac{\mu L Q_o}{A_o \Delta P}, \tag{2}$$

where L is the length of the sample or image, A_o corresponds to the outlet surface area, Q_o is the volumetric flow rate derived by integrating over the sample outlet surface area (A_o), and ΔP corresponds to the pressure gradient drop over the sample length. In addition to the permeability, the formation resistivity factor, which quantifies the effect of pore space on the sample's electrical resistance, is also computed. It is worth noting that the present work is applied to pores space consisting of pores without fractures, even though a recent paper discusses a potential extension to fractured porous media (Jiang et al., 2017).

2.2. Permeability computed by FVM

FVM is implemented to solve fluid flow equations within the porous media by discretizing the following mass and momentum conservation equations:

$$\nabla.\mathbf{V} = 0, \tag{3}$$

$$\rho\mathbf{V}\nabla\mathbf{V} = -\nabla p + \nabla.(\mu\nabla\mathbf{V}), \tag{4}$$

where $\mathbf{V}$ represents the velocity of an assumed-incompressible fluid of density ρ and viscosity μ.

The pore space was generated from the micro-CT image and meshed, details of which can be found in Tembely et al. (2017). Subsequently, the permeability was calculated using the relationship provided in Eq. (2).

2.3. Permeability computed by LBM

An LBM technique based on a single-time relaxation scheme and a Bhatnagar–Gross–Krook (BGK) model approximation of the collision term was used to compute the permeability. A fluid consisting of fictive particles of distribution $f(x, t)$ satisfies the following evolution equation:

$$f(x + e_i, t + 1) = \frac{1}{\tau}\left(f(x, t) - f_{eq}(x, t)\right) \tag{5}$$

where τ corresponds to the relaxation time and e_i is the particle velocity in the *ith* direction. Finally, the permeability was similarly established directly from the binary images, using Darcy's law from Eq. (2).

2.4. Numerical simulations

For a given image, we illustrate in Fig. 2 the approximation of the pore space used to perform numerical simulations by PNM, FVM, and LBM. LBM can be simulated directly on the 3D segmented images, while FVM requires a simplified pore space obtained by meshing, which is very challenging. PNM requires even further simplification of the pore geometry, and, as a result, both PNM and FVM can be deemed less reliable than LBM in the context of pore-scale simulation.

Regarding the numerical simulations, we considered subsamples (or images) extracted from the complex carbonate image provided in Fig. 1. In the context of applying ML model, we use "sample" to refer to each of the segmented 3D micro-CT images from our dataset. In order to use PNM on the segmented 3D images, we first extracted the network using the maximal ball algorithm described in Dong and Blunt (2009). Fig. 3 depicts the statistics of the pore structure from 3 samples, where the pore-network geometry is depicted in terms of the probability density function(PDF) of the pore diameter, throat diameter, and throat length, highlighting complex carbonate pore spaces covering a broad range of length scales.

To estimate the permeability properties, numerical simulations were performed using PNM, FVM, and LBM. Fig. 4 shows the schematic of the input geometry used by the three methods to estimate the permeability from a rock sample imaged at high resolution through X-ray microtomography, as applied to Sample 1 of the generated dataset,

We summarized the simulated values of the permeability for the three samples and three numerical techniques in Fig. 5.

While FVM and LBM are in good agreement, a discrepancy is noticeable for the PNM simulations, consistent with findings highlighted in Dong and Blunt (2009). In the present work, LBM is considered to be the ground truth for the permeability value of a given segmented image. As a result, the average error from

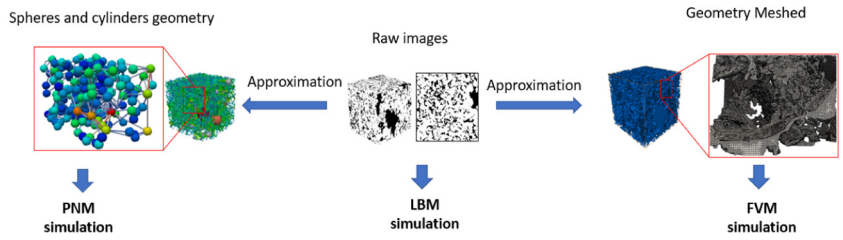

Fig. 2. Illustration of the pore geometry simplification from the micro-CT image required for PNM, LBM, and FVM simulations.

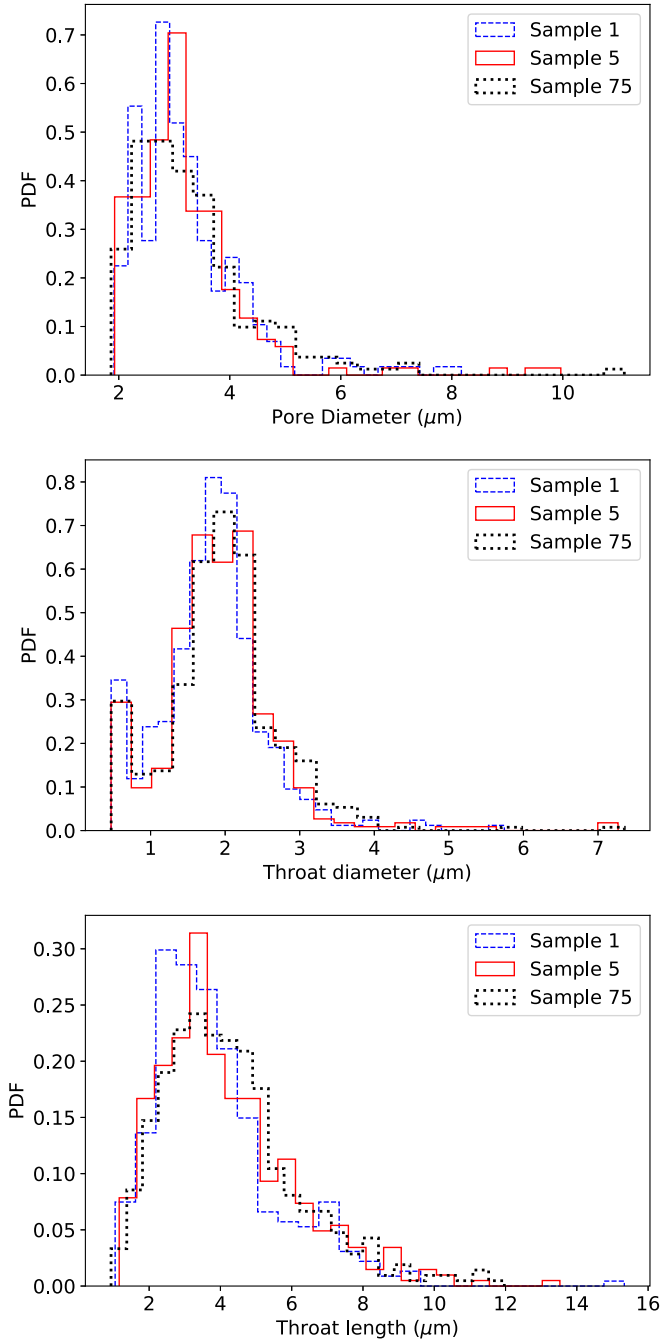

Fig. 3. Statistics of carbonate and sandstone pore-network extraction.

PNM is approximately 30%, while FVM yields an average error of roughly 13% with respect to the LBM results (Table 1).

Table 1
Comparative simulation of the permeability (in mD) using PNM, FVM and LBM based on three samples (or images).

Sample ♯	PNM (error)	FVM (error)	LBM
Sample 1	7.29 (29%)	4.93 (13%)	5.67
Sample 5	8.27 (34%)	10.99 (12%)	12.56
Sample 75	9.65 (35%)	12.66 (15%)	14.93

It should be noted that the computation time of the LBM simulation is more than an order of magnitude greater than that of the FVM simulation, while PNM executes the simulation run instantly once the pore network is generated, which is a relatively fast operation employing the modified maximal ball algorithm. Overall, the difference in computation time between LBM (∼2400 s) and PNM (∼1 s) is more than three orders of magnitude in CPU time. The main benefit of the PNM is that the simplified geometry makes it possible to efficiently simulate much larger 3D digital rock volumes. Although PNM may be less accurate due to the simplified pore space, a better understanding of fluid flow properties through porous media can readily be gained from it. Because of its simplicity, PNM is commonly used in pore-scale modeling to assess petrophysical properties from images. Our strategy of leveraging machine and deep learning for the estimation of permeability is detailed below.

3. Application of shallow and deep learning techniques

This section details the application of the different machine and deep learning algorithms after dataset generation, which is performed through extensive numerical simulations using both LBM and PNM in addition to images processing to determine the porosity. After tree-based models were explored, a deep learning algorithm was applied through deep neural network (DNN) and convolutional neural network (CNN) to the 3D micro-CT images.

3.1. Data generation and feature engineering

A dataset consisting of 1100 segmented images of 100 $\times$100 $\times$160 voxels was extracted from a complex carbonate rock and analyzed using ML (Fig. 1). Additionally, a dataset of 400 samples from the literature was considered for further validation of our approach. These images were provided by IFP under the 2018 AI Challenge. Due to its computational efficiency, the PNM technique is used in conjunction with image processing to generate the following input labels (or features) in the proposed ML model: porosity (PHI), median throat length to radius ratio (TR), average connection number (CN), permeability (KPNM) and formation resistivity factor (FF). The latter (FF) describes the influence of pore space on the electrical resistance of the porous media. It corresponds to the ratio of the resistivity of fully saturated rock to that of the saturating liquid (water), and represents the effect of the sample tortuosity as well as porosity. In addition to the engineered input features, direct simulations based on

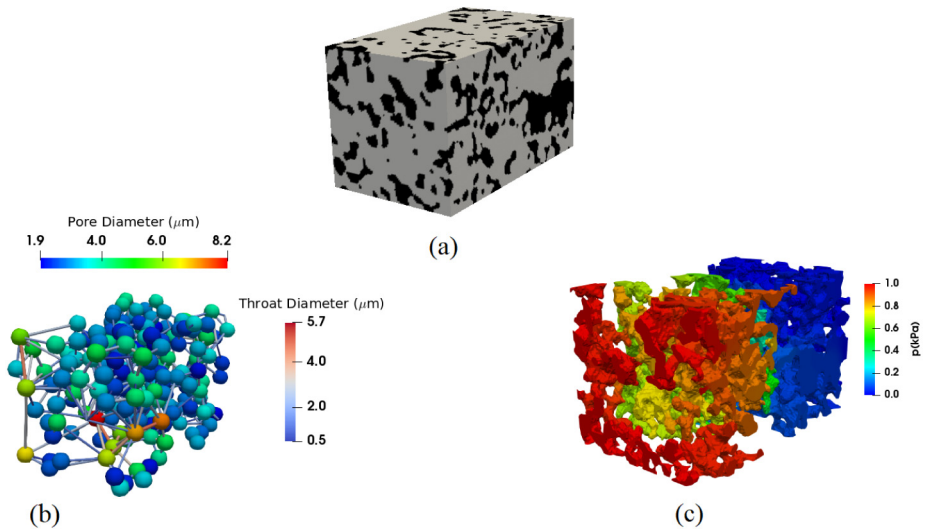

Fig. 4. Approach and geometry used for (a) LBM simulation on a binary image, (b) PNM simulation on the approximate pore network, and (c) FVM simulation on the meshed pore space from the 3D micro-CT image of Sample 1.

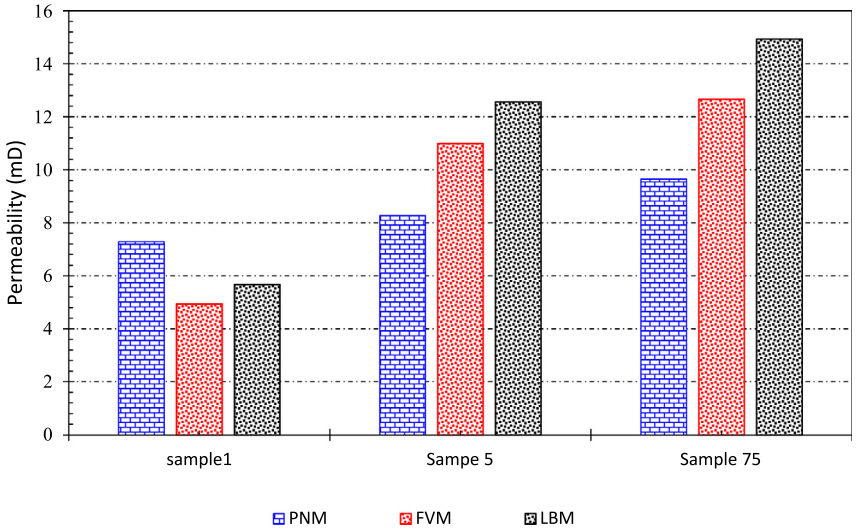

Fig. 5. The computed permeability of three samples based on PNM, FVM and LBM.

LBM were performed to compute the permeabilities (Klbm) of all 1100 samples. ML could reduce processing time substantially when compared to direct simulations with comparable accuracy. Finally, to evaluate the accuracy of our models, we used the R2-score, or coefficient of determination, to assess the predictive capability of the various algorithms tested. Finally, in order to ensure that weights of all features are equal in their representation, we performed data normalization using the mean ($\tilde{X}_F$) and standard deviation of the training set (σ_{X_F}) following the equation below:

$$X_{scaledF} = \frac{X_F - \tilde{X}_F}{\sigma_{X_F}} \tag{6}$$

We provide in Fig. 6 an overview of the dataset by presenting the cross-plot of relevant features as functions of the permeability as computed by the more accurate LBM technique; interestingly, the high variability of the different properties inherent to carbonate rock is retrieved by this method. The results emphasize that the PNM cannot accurately predict the actual sample permeability. Although the PNM is commonly used to model petrophysical properties, these findings indicate that its simplistic representation should be corrected for use as a predictive tool for rock permeability.

Interestingly, if we focus on the cross-correlation between the PNM and the LBM methods (Fig. 7), we observe that the predictive capability of the PNM is very limited for a complex carbonate, with a correlation coefficient R2-score of only 15.4%.

The aim of the present work was to improve the computation of permeability by PNM through the use of machine and deep learning. We have used both supervised (i) shallow learning techniques and (ii) deep (or artificial) neural networks to estimate the permeability from images. We first trained the learning models using the input (features) and output (permeability values) of the data previously generated, and subsequently used the model to predict the permeability of the remaining test dataset. Finally, with respect to the code implementation, it is worth noting that the supervised regression ML techniques were based on linear and tree-based models employing the scikit-learn library, while deep learning models were based on TensorFlow coupled with the Keras framework. The different codes used opensource packages and were implemented in C++/Python, OpenPNM, OpenFOAM, and Palabos.

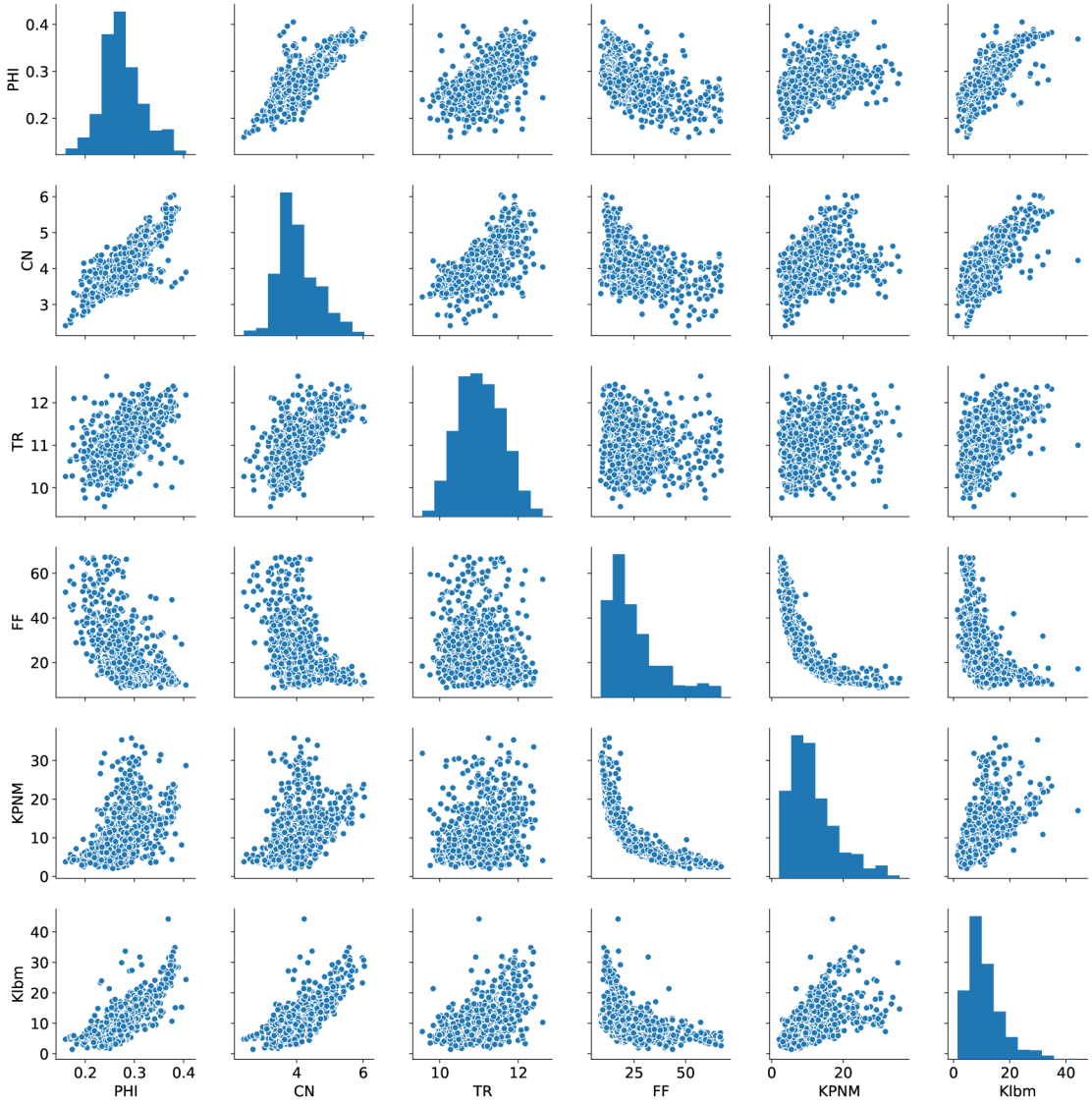

Fig. 6. Statistics of the generated data for machine learning purposes.

3.2. Prediction of permeability by machine and deep learning

3.2.1. Machine learning approach

Supervised machine learning requires training the system with input data (X) and ouput or label data (K), corresponding to the permeability in the present case. The permeability can be parametrized by a set of parameters ξ and the input feature (X), such that $K(X, \xi)$. The machine learning approach requires optimization of the following algorithms on ξ for a given label (y_i) from the training set:

$$\tilde{\xi}_i = arg \min_{\xi} \frac{1}{N} \sum_{i=1}^{N} L(y_i, K(X_i, \xi)) \tag{7}$$

In the case of linear regression, the label can be written as follows:

$$K(X, \xi) = w_0 x_0 + w_1 x_1 + \cdots + w_p x_p + b \tag{8}$$

where $\xi = (w, b)$ accounting for both the weights and biases parameters. In this case, the associated loss function (L), which has to be minimized, yielded:

$$L(w, b) = \frac{1}{N} \sum_{i=1}^{N} (y_i - K(X_i, \xi))^2 \tag{9}$$

In addition, we employed tree-based models such as random forest (RF) and gradient boost (GB) models, which are built using many independent decision trees to train and make predictions. It should be noted that boosting algorithms account for trees sequentially in such a way that the next estimator learns from the errors of the previous one. Finally, the deep learning approach for estimating the permeability is detailed below.

3.2.2. Supervised shallow learning

We used a supervised regression problem that aimed to estimate actual target values. We employed both linear and tree-based regression models; to improve these two approaches, feature-cross (FC) techniques are also investigated. Of the 1100 samples, 70% of the samples were used for training the learning algorithms, while the remaining 30% were held out for testing. After fitting the model on the training data, we obtained the results of the predictions made by using both linear regression (LR) and gradient boost (BG) techniques on the testing dataset

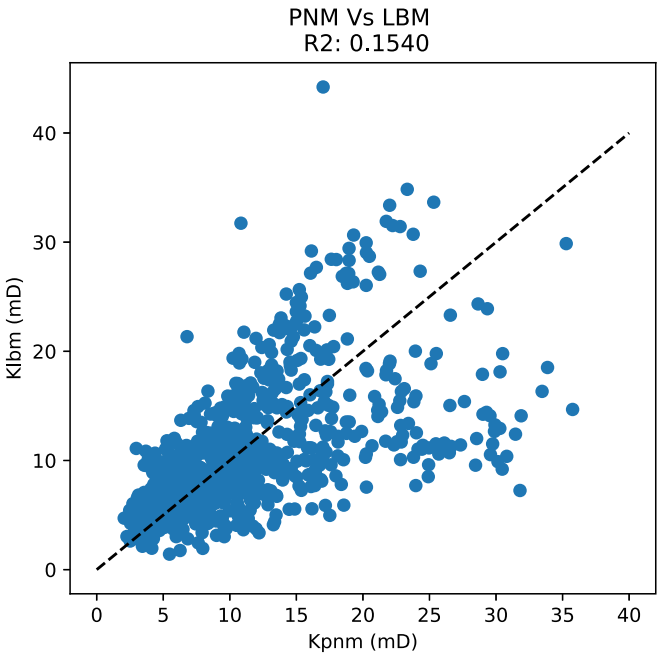

Fig. 7. Cross-plot of the permeability computed by the PNM and the LBM simulations from 3D images of carbonate rock.

(Fig. 8). From the two algorithms, we can observe a slightly better R2-score, of nearly 79.6% using the gradient boost model, compared to 73% using the linear model.

It is worth mentioning that the hyperparameters used for the model have been optimized and 5-fold cross-validated using grid-search. In the case of GB model, this led to the hyperparameters for the number of estimators and the learning rate presented in Fig. 9. We retained a learning rate of 0.1 and an estimator of 100 for the GB algorithm.

Finally, we used feature-cross techniques to boost the performance of the ML algorithm. The term feature-cross refers to a synthetic feature that encodes nonlinearity in the feature space by multiplying two or more input features together. We determined that the optimum feature-cross corresponded to polynomial combinations of the input features with a degree less than or equal to two for the GB technique (Fig. 10), showing

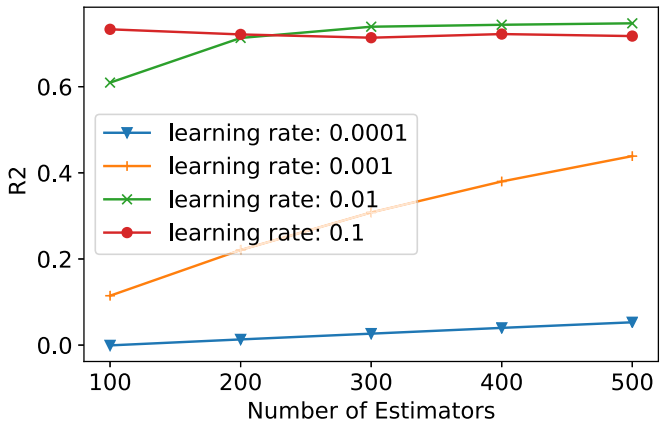

Fig. 9. Hyperparameters optimization analysis.

a better performance compared to the case in Fig. 8 excluding feature-cross.

Next, the performance was slightly improved to give an R2-score above 81% by using improved or extreme gradient boosting (XGB) and random forest (RF) algorithms (Fig. 11). It is worth noting that tree-based GB algorithms are more sensitive to overfitting and the hyperparameters are harder to tune. XGB, an optimized distributed GB, builds trees one at a time, where each new tree helps to correct errors made by the previously trained tree, leading to greater capability for generalization. The RF method with two primary parameters to tune (the number of trees and the number of features to be selected at each node) is less subject to overfitting, which may explain its relatively good performance. Finally, accounting for non-linear models such as tree-based algorithms (e.g., RF and GB, based on decision tree ensembles and weak learners) leads to a higher accuracy; this may also support an inherent non-linearity in carbonate rock between input features and output.

Additionally, we assessed the importance of features to the predictive ability of the proposed ML techniques. As shown in Fig. 12, we uncovered that the prominent input feature, interestingly, is the porosity, followed by the PNM permeability, the coordination number, to a lesser extent the formation factor and average pore-throat radius.

Finally, we analyzed sensitivity to additional features. In addition to the total porosity, we extracted the porosity profiles along

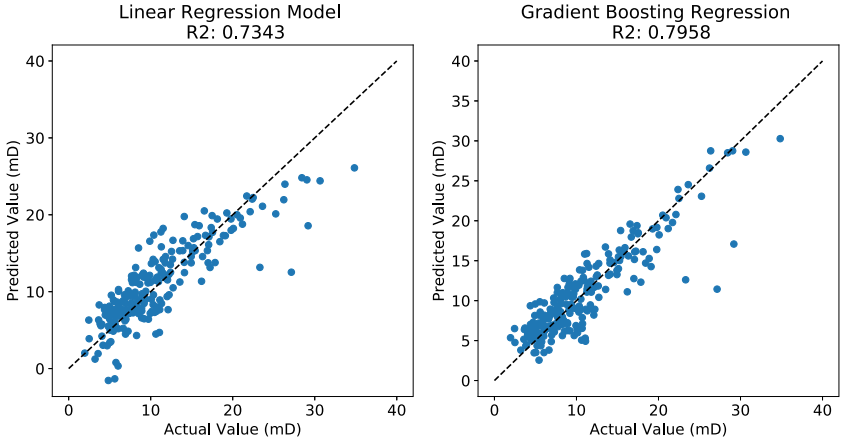

Fig. 8. The estimation of permeability using (left) LR and (right) GB regression algorithms, respectively.

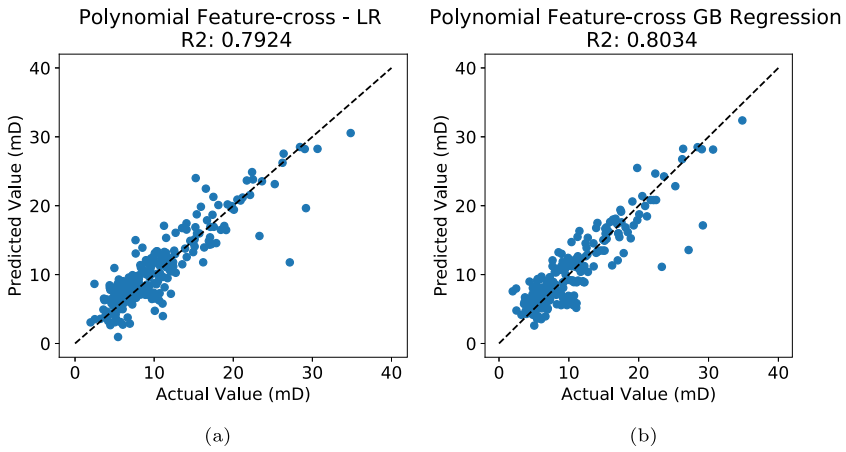

Fig. 10. Feature-cross using polynomial combinations of the input features with degree ≤ 2 for both (left) LR and (right) GB learning techniques.

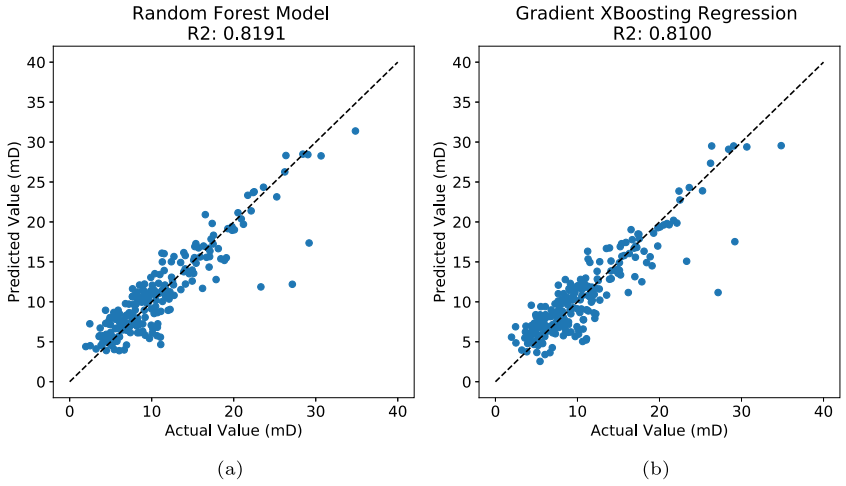

Fig. 11. The estimation of permeability using (left) RF regression and (right) improved (or XGB) gradient algorithms, respectively.

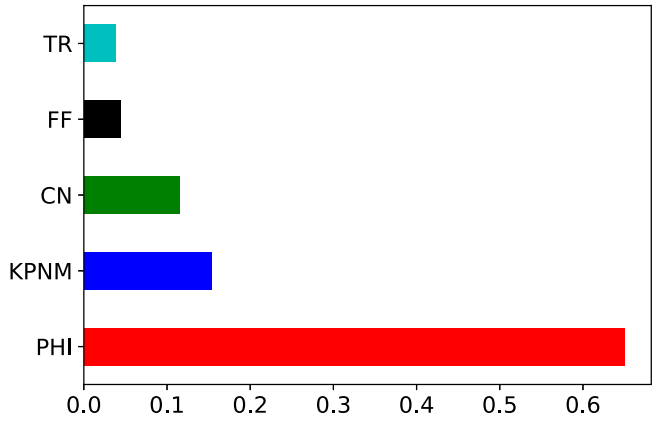

Fig. 12. Features importance.

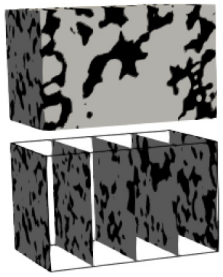

Fig. 13. Porosity profiles extracted per slice from a 3D micro-CT image. The case of porosity extracted along the z-axis is shown for Sample 1 of our dataset.

the 3 axes of the samples. We show in Fig. 13 the approach to extract the porosity profiles from a 3D micro-CT image along the z-axis.

The results from the 3 axes are shown in Fig. 14.

In the present case, we found and used as relevant features the porosity profiles along the sample z axis direction, in addition to KPNM and the porosity (PHI). The results are shown for the RF and XGB algorithms in Fig. 15. This additional feature leads to the model giving an improved R2-sore of 87% for RF, compared to the previous model (Fig. 11), which involved less complex features engineering.

One of the limitations of this approach is that the input features along the z-axis should be of the same size, and extension of the approach to other images of different sizes, for example, is not straightforward. As a result, although this approach can offer an improvement compared to the features adopted previously, we did not retain the extended features for the permeability prediction in the next section for generalizability.

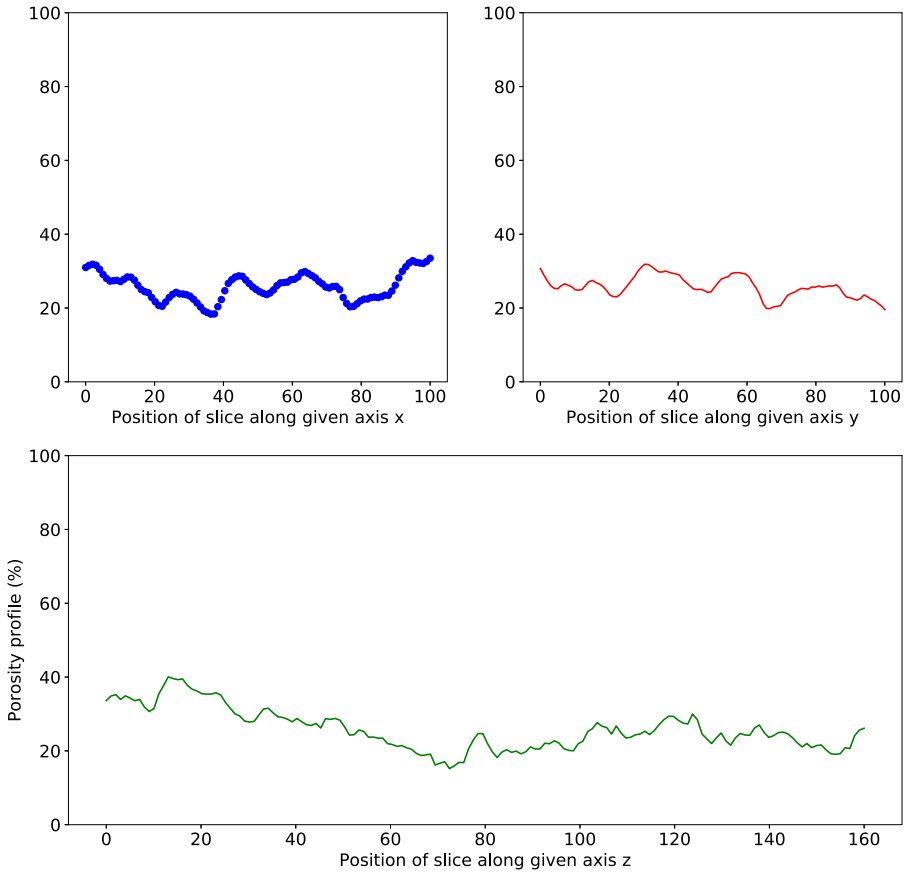

Fig. 14. The derived porosity profiles along the 3 axes, considered as features for the machine learning algorithms.

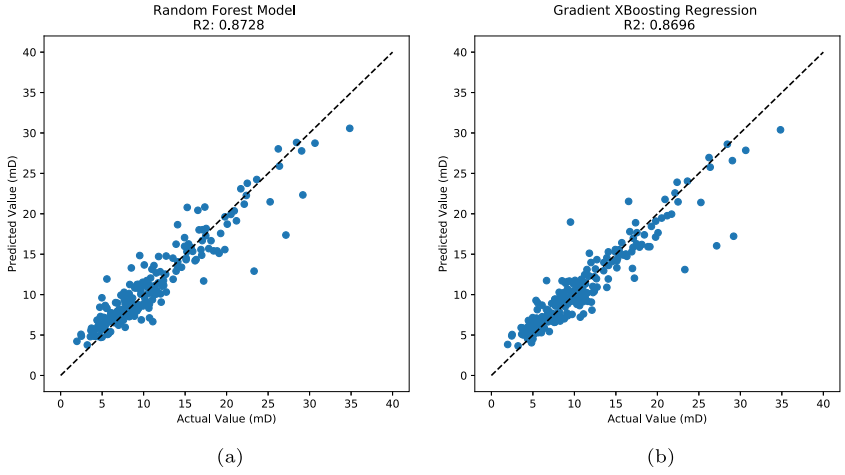

Fig. 15. The prediction of permeability using (left) RF and (right) XGB regression algorithms using the porosity profiles features.

3.2.3. Deep learning from a deep neural network

Here we employed deep learning, through an artificial neural network architecture known as a multilayer perceptron, to probe the permeability based on the input features previously extracted in the shallow learning analysis. An activation function was used to introduce non-linearity into the output of a neuron, so that the relationship between the input feature ($\boldsymbol{x}$) and target (or output) ($\boldsymbol{y}$) of a single hidden layer is expressed as follows:

$$y = \sigma[wx + b] \tag{10}$$

In the present study, an activation function based on the rectified linear unit (ReLU), σ, is adopted. Eq. (10) illustrates a neural network of a single hidden layer mapping the feature vector $\boldsymbol{x}$ to the output vector$\boldsymbol{y}$ through the bias, b, and weight, w. From a single neuron, a deep neural network (DNN) is constructed as sequential layers, consisting of interconnected nodes of multiple hidden layers, through which data flow. The architecture of our feed-forward base model of a densely-connected network, consisting of three hidden layers with 10 nodes each is depicted in Fig. 16.

The result of the prediction by the DNN is shown in Fig. 17, which provides better performance compared to the previous ML algorithms. We can expect even better performance with a larger dataset.

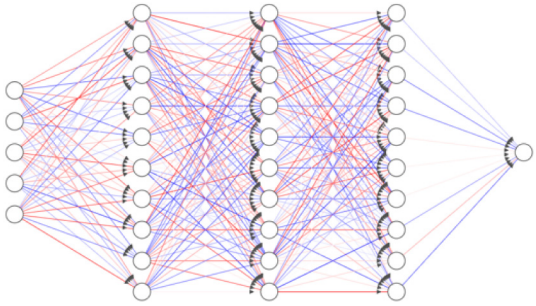

Fig. 16. Architecture used for the deep neural network model.

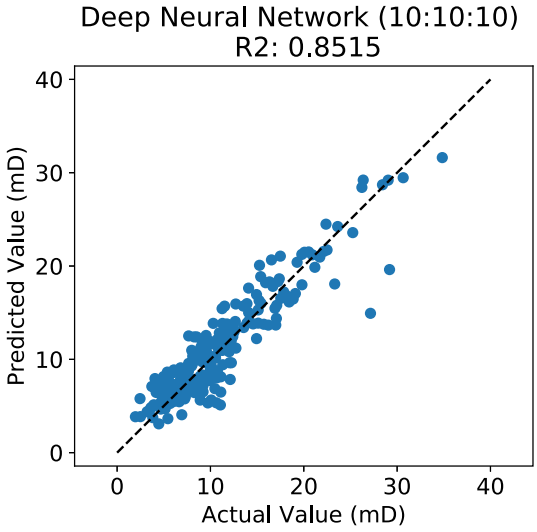

Fig. 17. Cross-plot of the permeability prediction by DNN based on 3D micro-CT images of the complex carbonate dataset.

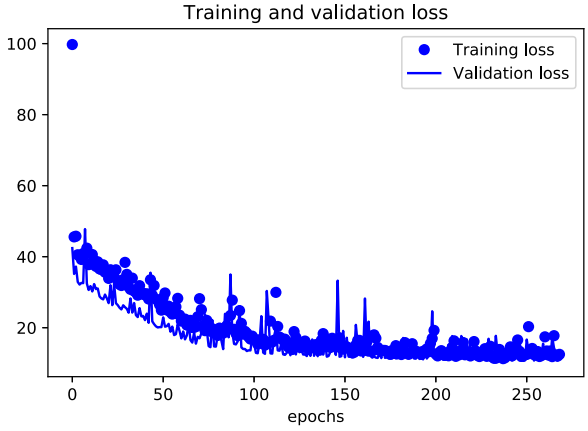

Fig. 18. The variation of the loss functions based on the training and validation set from the adopted DNN model.

It is worth noting that the DNN model was optimized from the architecture in Fig. 16 by employing the TensorBoard toolkit incorporated into TensorFlow. We ensured that the DNN model is not overfitted by closely monitoring the variation of the loss function and employing the early stopping technique. We show in Fig. 18 the variation of the loss function from the training and validation set in terms of the number of epochs, indicating that the DNN model is not overfitted.

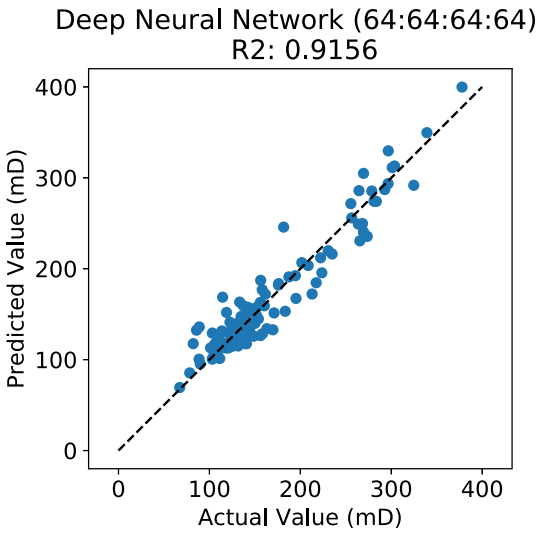

Fig. 19. Permeability prediction by DNN applied to the sandstone dataset.

Table 2
The architecture of CNN used.

CV	Kernel size = (5,5,5) Stride = (1,1,1) Activation = ReLU
POOL	Kernel size = (5,5,5) Stride = (1,1,1) Activation = ReLU
FC	Neurones = [8,16], [8,64,128] Activation = ReLU

Next, we tested the model on a new dataset from the literature consisting of 400 samples. The results for the optimized DNN are shown in Fig. 19, with an R2-score of more than 91%. It is worth noting that the technique can be applied to any rock sample scanned at high resolution.

Finally, we implemented a supervised CNN model which is a deep learning technique dealing with images (Valueva et al., 2020; LeCun et al., 1998). In traditional image processing, to extract a feature from an image, a filter matrix must be handcrafted. For example, to obtain the vertical edges for a given image, convolution is performed between the images and the filter to obtain the final representation consisting of the edge. In deep learning, the filters are instead obtained by training the network. Different filters can be applied to the images to build a CNN. Additionally, in CNN the number of parameters is reduced by sharing the weight of the convolution kernel (or filter) at different locations in the images. In addition to being space or shift-invariant, CNN is able to achieve similar or better performance with much less training data compared to regular neural networks. This model used only the grayscale segmented images and was not able to predict the permeability with an accuracy of more than 64%. The accuracy is measured by computing the R2-score between the prediction by CNN and the LBM results on the test dataset. The architecture of the CNN model is given in Table 2. The CNN consisted of two convolutional layers, one pooling layer, and three fully-connected layers (Fig. 20). To optimize the performance of the CNN model, we expanded it to include additional input features, such as the sample porosity, and formation factor which are added (or concatenated) to the CNN model as shown in Fig. 21. Although this model is more complete, we did not observe an improvement in terms of performance (Fig. 22). Again, the lack of a large set of data could explain the lack of improvement observed for deep learning based on the CNN model.

We show in Fig. 23 a summary of the R2-scores of the different algorithms used in the present study including linear regression(LR), support vector regression (SVR), and deep neural network (DNN). Interestingly, all the algorithms performed better than the PNM computation of the permeability.

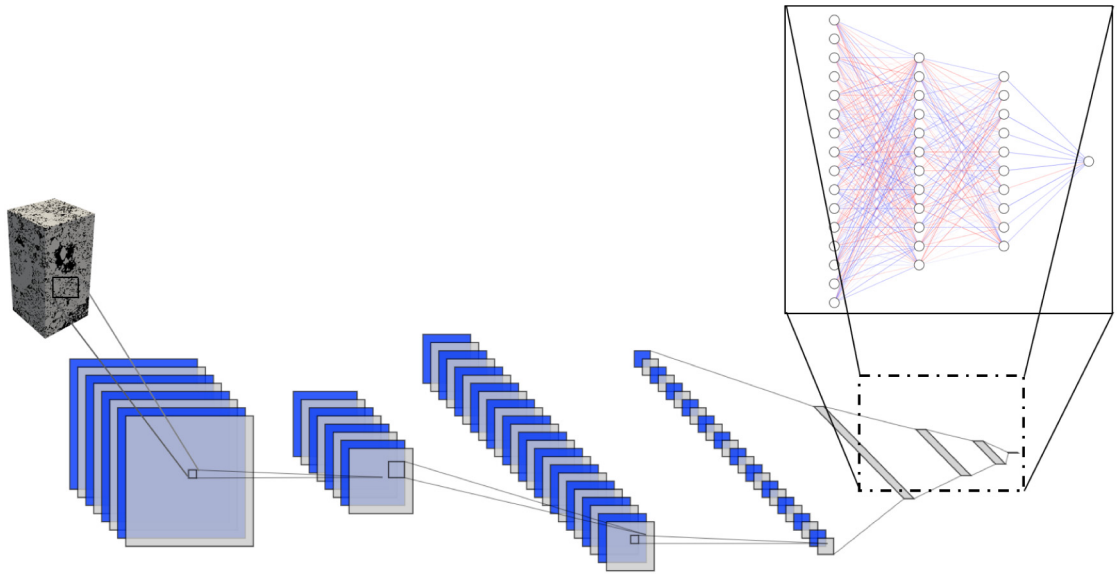

Fig. 20. Schematic of the CNN deep learning architecture for the permeability estimation.

Fig. 21. Detailed schematic of our physics-informed 3D-CNN architecture for the permeability prediction.

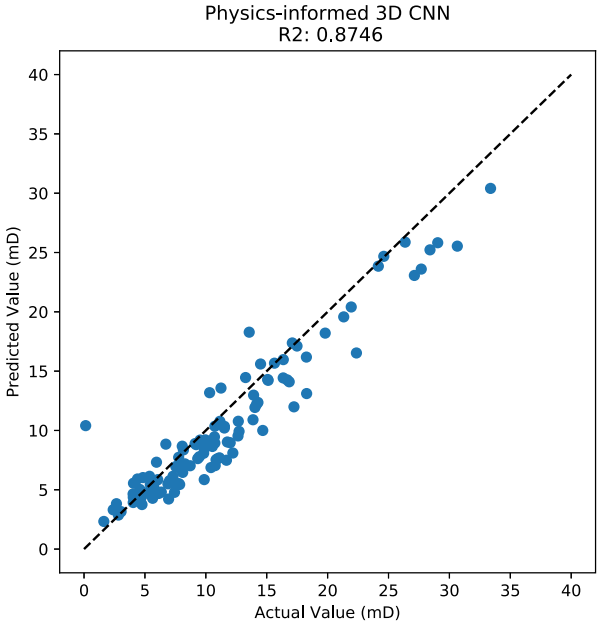

Fig. 22. A physics-informed CNN applied to a complex carbonate sample.

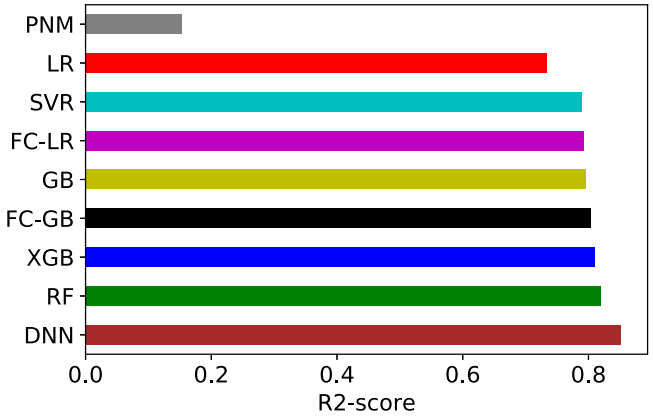

Fig. 23. Summary of R2-scores computed from the different machine and deep learning algorithms used in the present study.

Finally, while the model has only been trained on a small subset of 3D images of 100 × 100 × 160 voxels, when we applied it to a larger volume of 500 × 500 × 920 voxels by extracting its features, the ML provided a permeability of 12.03 mD in less than a second compared to the value of 12.38 mD obtained by running the LBM simulation for a day. This highlights the capability of ML to accurately estimate (within 3% error) complex and heterogeneous rock permeability. Finally, further work and data will be required for a universal solver to generalize the approach to images at different resolutions and rock types.

4. Conclusion

The recent advent of machine and deep learning models capable of detecting hidden patterns and features from images has revolutionized AI fields. In this context, this paper developed a new method to estimate petrophysical properties based on X-ray micro-CT scans. We developed a workflow for a quick, efficient and accurate prediction of the permeability of complex carbonate rock from the Middle East. This data-driven approach is based on machine and deep learning in conjunction with numerical techniques, including the pore-network and lattice Boltzmann techniques. While both PNM and LBM can estimate permeability from micro-CT images, PNM requires the geometry for a given image to be approximated using geometric primitives, such as spheres and cylinders, whereas LBM does not need any simplification. As a result, PNM is less accurate than LBM, whose governing equations recover Navier–Stokes equations. To benefit

from the fast and efficient simulation by PNM and the accuracy of the LBM, various supervised learning techniques have been investigated to estimate the permeability of rock scanned at high resolution. Both linear and tree-based regression models have been tested on a dataset containing more than a thousand micro-CT 3D images, from which relevant input features such as the formation resistivity factor and porosity are extracted and fed into supervised shallow and deep learning models to estimate the permeability. The deep neural network is found to perform slightly better than gradient boosting and linear regression with feature crossing. Finally, after training and validation, the AI-based model estimated the permeability three orders of magnitude faster compared to direct simulation. The results provided a framework for estimating the petrophysical properties of rock samples based on X-ray micro-CT scans. With our data-driven workflow, simulations that could take days will require just a few seconds to complete. For perspective, the predictions made by convolution neural networks based solely on grayscale 3D images could be improved to help minimize the features engineering involved in ML to estimate the permeability. Finally, future work could involve extending the current AI model for transfer learning based on the mapping between low-resolution 3D images to their respective petrophysical properties.

CRediT authorship contribution statement

Moussa Tembely: Designed the study, Performed the study, Wrote the paper. **Ali M. AlSumaiti:** Designed the study. **Waleed S. Alameri:** Designed the study.

Declaration of competing interest

The authors declare that they have no known competing financial interests or personal relationships that could have appeared to influence the work reported in this paper.

References

Alkinani, H.H., Al-Hameedi, A.T.T., Dunn-Norman, S., Flori, R.E., Alsaba, M.T., Amer, A.S., 2019. Applications of artificial neural networks in the petroleum industry: A review. In: SPE Middle East Oil and Gas Show and Conference, MEOS, Proceedings, Vol. 2019-March. http://dx.doi.org/10.2118/195072-ms, URL https://www.onepetro.org/download/conference-paper/SPE-195072-MS?id=conference-paper%2FSPE-195072-MS.

Alpak, F.O., Zacharoudiou, I., Berg, S., Dietderich, J., Saxena, N., 2019. Direct simulation of pore-scale two-phase visco-capillary flow on large digital rock images using a phase-field lattice Boltzmann method on general-purpose graphics processing units. Comput. Geosci. 23 (5), 849–880. http://dx.doi.org/10.1007/s10596-019-9818-0.

Andrä, H., Combaret, N., Dvorkin, J., Glatt, E., Han, J., Kabel, M., Keehm, Y., Krzikalla, F., Lee, M., Madonna, C., Marsh, M., Mukerji, T., Saenger, E.H., Sain, R., Saxena, N., Ricker, S., Wiegmann, A., Zhan, X., 2013. Digital rock physics benchmarks-part II: Computing effective properties. Comput. Geosci. 50, 33–43. http://dx.doi.org/10.1016/j.cageo.2012.09.008.

Araya-Polo, M., Alpak, F.O., Hunter, S., Hofmann, R., Saxena, N., 2020. Deep learning–driven permeability estimation from 2D images. Comput. Geosci. 24 (2), 571–580. http://dx.doi.org/10.1007/s10596-019-09886-9.

Blunt, M.J., Bijeljic, B., Dong, H., Gharbi, O., Iglauer, S., Mostaghimi, P., Paluszny, A., Pentland, C., 2013. Pore-scale imaging and modelling. Adv. Water Resour. 51, 197–216. http://dx.doi.org/10.1016/j.advwatres.2012.03.003.

Brunton, S.L., Noack, B.R., Koumoutsakos, P., 2020. Machine learning for fluid mechanics. Annu. Rev. Fluid Mech. 52, 477–508. http://dx.doi.org/10.1146/annurev-fluid-010719-060214, URL https://www.annualreviews.org/doi/abs/10.1146/annurev-fluid-010719-060214.

Chilamkurthy, S., Ghosh, R., Tanamala, S., Biviji, M., Campeau, N.G., Venugopal, V.K., Mahajan, V., Rao, P., Warier, P., 2018. Deep learning algorithms for detection of critical findings in head ct scans: a retrospective study. Lancet 392 (10162), 2388–2396. http://dx.doi.org/10.1016/S0140-6736(18)31645-3, URL http://www.thelancet.com/article/S0140673618316453/fulltexthttp://www.thelancet.com/article/S0140673618316453/abstracthttps://www.thelancet.com/journals/lancet/article/PIIS0140-6736(18)31645-3/abstract.

Chung, T., Wang, Y.D., Armstrong, R.T., Mostaghimi, P., 2019. Approximating permeability of microcomputed-tomography images using elliptic flow equations. SPE J. 24 (3), 1154–1163. http://dx.doi.org/10.2118/191379-PA, URL https://www.onepetro.org/download/journal-paper/SPE-191379-PA?id=journal-paper%2FSPE-191379-PA.

Davarpanah, A., Mirshekari, B., Jafari Behbahani, T., Hemmati, M., 2018. Integrated production logging tools approach for convenient experimental individual layer permeability measurements in a multi-layered fractured reservoir. J. Pet. Explor. Prod. Technol. 8 (3), 743–751. http://dx.doi.org/10.1007/s13202-017-0422-3.

Davarpanah, A., Mirshekari, B., Razmjoo, A., 2020. A parametric study to numerically analyze the formation damage effect. Energy Explor. Exploit. 38 (2), 555–568. http://dx.doi.org/10.1177/0144598719873094, URL http://journals.sagepub.com/doi/10.1177/0144598719873094.

Dehghan Khalili, A., Arns, J.Y., Hussain, F., Cinar, Y., Pinczewski, W.V., Arns, C.H., 2013. Permeability upscaling for carbonates from the pore scale by use of multiscale X-ray-CT images. SPE Reserv. Eval. Eng. 16 (4), 353–368. http://dx.doi.org/10.2118/152640-PA, URL http://www.onepetro.org/doi/10.2118/152640-PA.

Dong, H., Blunt, M.J., 2009. Pore-network extraction from micro-computerized-tomography images. Phys. Rev E - Statist. Nonlinear Soft Matter Phys. 80 (3), 1–11. http://dx.doi.org/10.1103/PhysRevE.80.036307.

Guibert, R., Nazarova, M., Horgue, P., Hamon, G., Creux, P., Debenest, G., 2015. Computational permeability determination from pore-scale imaging: Sample size, mesh and method sensitivities. Transp. Porous Media 107 (3), 641–656. http://dx.doi.org/10.1007/s11242-015-0458-0.

Hu, X., Xie, J., Cai, W., Wang, R., Davarpanah, A., 2020. Thermodynamic effects of cycling carbon dioxide injectivity in shale reservoirs. J. Pet. Sci. Eng. 195, 107717. http://dx.doi.org/10.1016/j.petrol.2020.107717.

Jiang, Z., van Dijke, M.I., Geiger, S., Ma, J., Couples, G.D., Li, X., 2017. Pore network extraction for fractured porous media. Adv. Water Resour. 107, 280–289. http://dx.doi.org/10.1016/j.advwatres.2017.06.025.

Kohli, A., Arora, P., 2014. Application of artificial neural networks for well logs. In: Society of Petroleum Engineers - International Petroleum Technology Conference 2014, IPTC 2014: Unlocking Energy Through Innovation, Technology and Capability, Vol. 3. pp. 2276–2283. http://dx.doi.org/10.2523/iptc-17475-ms, URL https://www.onepetro.org/download/conference-paper/IPTC-17475-MS?id=conference-paper%2FIPTC-17475-MS.

LeCun, Y., Bottou, L., Bengio, Y., Haffner, P., 1998. Gradient-based learning applied to document recognition. Proc. IEEE 86 (11), 2278–2323. http://dx.doi.org/10.1109/5.726791.

Ling, K., 2012. Correlation between rock permeability and formation resistivity factor-a rigorous and theoretical derivation. In: Society of Petroleum Engineers - SPE Middle East Unconventional Gas Conference and Exhibition 2012, UGAS - Unlocking Unconventional Gas: New Energy in the Middle East. Society of Petroleum Engineers, pp. 459–468. http://dx.doi.org/10.2118/152724-ms.

Mandal, P.P., Rezaee, R., 2019. Facies classification with different machine learning algorithm – an efficient artificial intelligence technique for improved classification. ASEG Ext. Abstr. 2019 (1), 1–6. http://dx.doi.org/10.1080/22020586.2019.12072918, URL https://www.tandfonline.com/doi/abs/10.1080/22020586.2019.12072918.

Miao, X., Gerke, K.M., Sizonenko, T.O., 2017. A new way to parameterize hydraulic conductances of pore elements: A step towards creating pore-networks without pore shape simplifications. Adv. Water Resour. 105, 162–172. http://dx.doi.org/10.1016/j.advwatres.2017.04.021.

Mostaghimi, P., Blunt, M.J., Bijeljic, B., 2013. Computations of absolute permeability on micro-CT images. Math. Geosci. 45 (1), 103–125. http://dx.doi.org/10.1007/s11004-012-9431-4.

Nwachukwu, A., Jeong, H., Pyrcz, M., Lake, L.W., 2018. Fast evaluation of well placements in heterogeneous reservoir models using machine learning. J. Pet. Sci. Eng. 163, 463–475. http://dx.doi.org/10.1016/j.petrol.2018.01.019, URL https://www.sciencedirect.com/science/article/pii/S0920410518300226.

Pereira, G.G., Prakash, M., Cleary, P.W., 2011. SPH Modelling of fluid at the grain level in a porous medium. Appl. Math. Model. 35 (4), 1666–1675. http://dx.doi.org/10.1016/j.apm.2010.09.043.

Pollock, J., Stoecker-Sylvia, Z., Veedu, V., Panchal, N., Elshahawi, H., 2018. Machine learning for improved directional drilling. In: Proceedings of the Annual Offshore Technology Conference, Vol. 4. pp. 2496–2504. http://dx.doi.org/10.4043/28633-ms, URL https://www.onepetro.org/download/conference-paper/OTC-28633-MS?id=conference-paper%2FOTC-28633-MS.

Rabbani, A., Babaei, M., 2019. Hybrid pore-network and lattice-Boltzmann permeability modelling accelerated by machine learning. Adv. Water Resour. 126, 116–128. http://dx.doi.org/10.1016/j.advwatres.2019.02.012.

Serre, T., 2019. Deep learning: The good, the bad, and the ugly. Annu. Rev. Vis. Sci. 5 (1), 399–426. http://dx.doi.org/10.1146/annurev-vision-091718-014951, URL https://www.annualreviews.org/doi/10.1146/annurev-vision-091718-014951.

Sudakov, O., Burnaev, E., Koroteev, D., 2019. Driving digital rock towards machine learning: Predicting permeability with gradient boosting and deep neural networks. Comput. Geosci. 127, 91–98. http://dx.doi.org/10.1016/j.cageo.2019.02.002.

Sun, S., Zhou, M., Lu, W., Davarpanah, A., 2020. Application of symmetry law in numerical modeling of hydraulic fracturing by finite element method. Symmetry 12 (7), 1122. http://dx.doi.org/10.3390/sym12071122, URL https://www.mdpi.com/2073-8994/12/7/1122.

Tembely, M., AlSumaiti, A.M., Alameri, W., 2020. A deep learning perspective on predicting permeability in porous media from network modeling to direct simulation. Comput. Geosci. 24 (4), 1541–1556. http://dx.doi.org/10.1007/s10596-020-09963-4.

Tembely, M., AlSumaiti, A.M., Jouini, M.S., Rahimov, K., 2017. The effect of heat transfer and polymer concentration on non-Newtonian fluid from pore-scale simulation of rock X-ray micro-CT. Polymers 9 (10), 509. http://dx.doi.org/10.3390/polym9100509, URL http://www.mdpi.com/2073-4360/9/10/509.

Valueva, M.V., Nagornov, N.N., Lyakhov, P.A., Valuev, G.V., Chervyakov, N.I., 2020. Application of the residue number system to reduce hardware costs of the convolutional neural network implementation. Math. Comput. Simulation 177, 232–243. http://dx.doi.org/10.1016/j.matcom.2020.04.031.

Wang, H., Yin, Y., Hui, X., Bai, J., Qu, Z., 2020. Prediction of effective diffusivity of porous media using deep learning method based on sample structure information self-amplification. Energy AI 2, 100035. http://dx.doi.org/10.1016/j.egyai.2020.100035.

Wu, J., Yin, X., Xiao, H., 2018. Seeing permeability from images: fast prediction with convolutional neural networks. Sci. Bull. 63 (18), 1215–1222. http://dx.doi.org/10.1016/j.scib.2018.08.006.

Xie, C., Zhang, J., Bertola, V., Wang, M., 2016. Lattice Boltzmann modeling for multiphase viscoplastic fluid flow. J. Non-Newton. Fluid Mech. 234, 118–128. http://dx.doi.org/10.1016/j.jnnfm.2016.05.003.

Yala, A., Lehman, C., Schuster, T., Portnoi, T., Barzilay, R., 2019. A deep learning mammography-based model for improved breast cancer risk prediction. Radiology 292 (1), 60–66. http://dx.doi.org/10.1148/radiol.2019182716.